



OPEN

SUBJECT AREAS:
ELECTRONIC PROPERTIES
AND MATERIALS
NANOSCALE MATERIALS
ELECTROCHEMISTRY
BATTERIESReceived
24 April 2013Accepted
15 July 2013Published
30 July 2013Correspondence and
requests for materials
should be addressed to
X.H. (xhuang@ntu.
edu.sg) or H.H.H.
(ashhng@ntu.edu.sg)

Carbon inverse opal entrapped with electrode active nanoparticles as high-performance anode for lithium-ion batteries

Xin Huang, Jing Chen, Ziyang Lu, Hong Yu, Qingyu Yan & Huey Hoon Hng

School of Materials Science and Engineering, Nanyang Technological University, 50 Nanyang Avenue, Singapore 639798, Singapore.

Enhancing ion and electron transport kinetics together with improving cycle life are important issues to be considered when developing high-performance Li ion batteries. Here we demonstrate a three dimensional ordered macroporous conductive electrode concept by entrapping electrode active nanoparticles in an interpenetrating macroporous carbon inverse opal. The electrodes are featured with simultaneously enhanced ion and electron transport kinetics as well as geometrically constrained active nanoparticles. The electrode can deliver up to 94.17% of theoretical capacity over 1000 discharge/charge cycles at a current density of 2.0 A g^{-1} , and exhibits good rate capability in the high current density range of $1.0\text{--}10.0 \text{ A g}^{-1}$. We hope that our findings will help pave the way for tailored design of many other sophisticated electrode materials in electrochemistry.

High performance Li ion batteries (LIBs) are required to deliver high capacity and cycling stability at high current density^{1,2}. To achieve these purposes, it is important to enhance the ion and electron transport kinetics as well as the stability of electrode active materials^{3–6}. Nanotechnology together with carbon coating provides the possibility to fulfill these requirements^{7–10}. As demonstrated, carbon-coated electrode active nanomaterials indeed exhibit improved rate capabilities and cycling stability due to the much smaller diffusion length and increased fracture strength compared to the bulk counterparts^{11–14}. For these materials, fast transport kinetics have been achieved in one dimensional (1D) carbon nanotube- and two dimensional (2D) graphene nanosheet-based hybrid electrodes^{15–18}. However in 1D and 2D electrodes, the fast electron transport is restricted at least in one dimension because of the structural anisotropy of the electrodes^{19–21}. As a result, the ambipolar (ionic and electronic) diffusion will be strictly constrained along that dimension, which eventually slows down the transport kinetics in the entire battery. Such kinetics problems will become more severe, especially at high current densities.

Ideally, the electrode should consist of an ordered three-dimensional (3D) interconnected network, where a 3D continuous transport pathway allows fast ion and electron transport without constrained ambipolar diffusion in any dimension. Along this line, initial strides have been made to fabricate three-dimensional ordered macroporous (3DOM) electrodes by colloid templating, such as $\text{Li}_4\text{Ti}_5\text{O}_{12}$ ²², SnO_2 ²⁰ and TiO_2 ²³. These electrodes indeed show promising potential in enhancing transport kinetics of batteries but only moderate rate performances and cycling stability are observed due to the fact that the macroporous structure mainly addresses ion transport rather than electron transport. In response to this challenge, that is, to afford the 3DOM electrodes better electronic conductivity, bicontinuous 3DOM electrode concept is proposed by depositing a layer of electrode active materials on pre-prepared 3DOM conductive inverse opal (e.g. carbon or nickel) or coating the 3DOM active materials with carbon materials^{5,24,25}. Although these bicontinuous electrodes enable high initial capacity and remarkable rate capabilities, they are still unable to provide a long-term cycling stability. Due to the lack of geometrical constraints in these electrodes, the pulverized active materials induced by cracking inside the active layer will inevitably peel off, eventually leading to cycling instability. Structural stability of the active materials is a critical factor in achieving a long cycle life. This issue is very challenging, and has not been well addressed. Owing to the above obstacles, the synthesis of ideal electrodes with fast electron and ion transport, as well as high cycling



stability would require new designing concepts that have a comprehensive consideration of all important issues in batteries, such as electrode architecture and configuration of active species.

Based on these considerations, we here report a new electrode concept that is based on the integration of a 3DOM carbon inverse opal with geometrically entrapped active nanoparticles (NPs). This concept is designed to simultaneously address the issues of transport kinetics and long-term cycling stability of batteries. Our proof-of-concept studies are based on the fabrication of 3DOM carbon inverse opal entrapped with SnO₂ NPs (SnO₂@3DOM) and CoO NPs (CoO@3DOM). In this design, the 3DOM carbon inverse opal ensures an interconnected continuous conductive network for fast electron transport, and the nanometer thick walls provide short diffusion pathways for lithium ions to go through. More importantly, the ordered periodic structure of the electrode minimizes the anisotropy of ion and electron transport kinetics because of the intrinsically geometric symmetry of the electrode. The macropores of the inverse opal also afford an easy accessibility of Li ions, and the geometrical constrains of elastic carbon inverse opal can accommodate the volume changes of oxide nanoparticles upon Li⁺ insertion/extraction, completely circumventing the self-aggregation and peeling off of the active materials.

Results

Synthesis and characterization of the SnO₂@3DOM electrode.

Colloidal crystal templating (CCT) is a versatile method to fabricate 3DOM architecture. Self-assembled silica, polystyrene (PS) and poly(methyl methacrylate) (PMMA) spheres are typically used as opal templates^{26–28}. Precursors fill the void spaces in opal templates by capillary action, and when the templates are removed via heating or chemical leaching, an ordered 3DOM inverse opal structure can be revealed. Although the synthesis of 3DOM electrodes is conceptually simple, the key issue in achieving perfect inverse opal replicas is homogeneous infiltration of precursors in the void spaces of templates. The poor wetting of precursors to templates will cause the replicas to lose their interconnectivity feature²⁹. Bearing this in mind, we choose self-assembled carboxylic polystyrene (COOH-PS) spheres with diameter of 240 nm as opal templates (Supplementary Fig. S1), and tannic acid-Sn⁴⁺ (TA-Sn⁴⁺) complexes (Supplementary Fig. S2) as the precursors of carbon and SnO₂. Since tannic acid has abundant phenolic hydroxyls, these complexes are able to interact with the carboxyl groups (COOH-) of the templates via intensive hydrophilic interactions^{30,31}, thus promoting the homogeneous distribution of TA-Sn⁴⁺ precursors on the templates. To prevent the swelling of colloidal crystal during infiltration, deionized water is used as the solvent instead of organic solvent. Other experimental parameters, such as calcination temperature and precursors dosage, have been optimized in order to achieve inverse opal with nanometer thickness walls. Vacuum annealing removes the COOH-PS opal template and allows the *in-situ* crystallization of SnO₂. Simultaneously, tannic acid decomposes to carbon inverse opal due to its low decomposition temperature according to TGA analysis (Supplementary Fig. S3). A schematic diagram illustrating the synthesis route of 3DOM-SnO₂ is shown in Figure 1. The inverse replica typically inherits the face-centered cubic (fcc) symmetry of the COO-PS sphere array. The fcc macropore array is interconnected through windows where templating spheres are in direct contact. Note that the *in-situ* formed SnO₂ NPs are spatially entrapped in the carbon inverse opal. The geometrical constrains of carbon inverse opal to the SnO₂ NPs not only ensure an interpenetrating continuous network for ion and electron transport, but also minimize the peel off of the active materials from electrode. In addition, the entire electrode is geometrically symmetric in three dimensions that will be beneficial for fast ion and electron transport in all directions. Our synthesis procedures are flexible to prepare other metal oxide-entrapped 3DOM electrodes because of the versatile chelating

ability of tannic acid towards transition-metal ions, and this is discussed in detail below.

Field emission scanning electron microscopy (FESEM) images in Figure 2a–c reveal that the SnO₂@3DOM exhibits highly ordered porous inverse opal structure, which has two types of periodic porosities, including large macropores with diameter of 220 nm formed by the COOH-PS spheres, and smaller mesopores with diameter of 40 nm formed by the contact points between the COOH-PS spheres. The wall thickness of the inverse opal is around 20 nm. The geometrical constrains of SnO₂ NPs in the carbon inverse opal are evident in the field emission transmission electron microscopy (FE-TEM) images. In Figure 2d–f, the interconnected carbon inverse opal is orderly packed, and small SnO₂ NPs are entrapped in the entire framework. The macroporous framework consists of very thin amorphous carbon wall, and the entrapped SnO₂ NPs with diameter of 4 ~ 10 nm are quite well dispersed (Figure 2f). High resolution TEM (HR-TEM) image of the SnO₂ NPs in Figure 2g shows the lattice spacing of 2.3 Å corresponding to the {111} plane of tetragonal SnO₂ (JCPDS No. 41-1445), and the polycrystalline nature of these NPs is confirmed by the selected area electron diffraction (SAED) (Figure 2h). The presence of tetragonal SnO₂ in SnO₂@3DOM is also identified by X-ray diffraction (XRD) patterns analysis (Supplementary Fig. S4), and the existence of the carbon framework is demonstrated by SEM-energy dispersive X-ray (SEM-EDX) (Supplementary Fig. S5) and Raman spectra (D band and G band of carbon materials are observed in Figure 2i). The differences in the mapping images of C, Sn and O further confirm the geometrical entrapment of SnO₂ NPs in carbon inverse opal. In Figure 2j–l, the mapping image of C element covers the entire inverse opal with a continuous distribution while the distributions of Sn and O elements are segregated into clusters. Actually, the carbon materials constitute the entire host so their signals cover the whole area of inverse opal while the SnO₂ NPs are just entrapped in the carbon host, thus showing discrete distribution.

Li ion batteries performances of the SnO₂@3DOM electrode. The LIBs performances of the SnO₂@3DOM were investigated using coin-type half-cells with a Li counter electrode and reference electrode. The cyclic voltammogram (CV) curves of the SnO₂@3DOM for the first 5 cycles are shown in Figure 3a. The CV curves from the 2nd to 5th cycle share similar shape but there are some differences between the 1st and subsequent cycles. As previously demonstrated^{32,33}, the electrochemical interaction between lithium and SnO₂ includes two steps given by the reactions: SnO₂ + 4Li⁺ + 4e⁻ → Sn + 2Li₂O (1); Sn + xLi⁺ + xe⁻ ↔ Li_xSn (0 < x ≤ 4.4) (2). In the first CV curve, the reduction peak at 0.95 should be attributed to the formation of a solid electrolyte interface (SEI) layer and Li₂O. The sharp reduction peaks below 0.5 V during subsequent discharging and the oxidation peaks at 0.51 V and 1.27 V during charging correspond to the reversible formation of Li_xSn alloys^{33,34}. Figure 3b shows the cycling stability of SnO₂@3DOM for 500 discharge/charge cycles at a current density of 0.5 A g⁻¹. In the 1st cycle, the discharge and charge capacities of SnO₂@3DOM are 1659.0 and 825.5 mAh g⁻¹, respectively, corresponding to a coulombic efficiency of 49.76%. The irreversible capacity should be mainly caused by the formation of SEI films on porous framework of the electrode although this could be improved by pre-lithiation in future optimization. In the 2nd cycle, the corresponding coulombic efficiency quickly increases from 49.76% to 91.95%, and the SnO₂@3DOM delivers a high reversible capacity of 759.6 mAh g⁻¹. In the 500th cycle, a high reversible capacity of 715.2 mAh g⁻¹ is still achieved, which retains 94.15% reversible capacity of the 2nd cycle, accounting for 91.57% of the theoretical capacity of SnO₂. Apparently, the SnO₂@3DOM presents excellent cycling stability without any significant capacity loss at a current density of 0.5 A g⁻¹. These results are superior to those reported for SnO₂

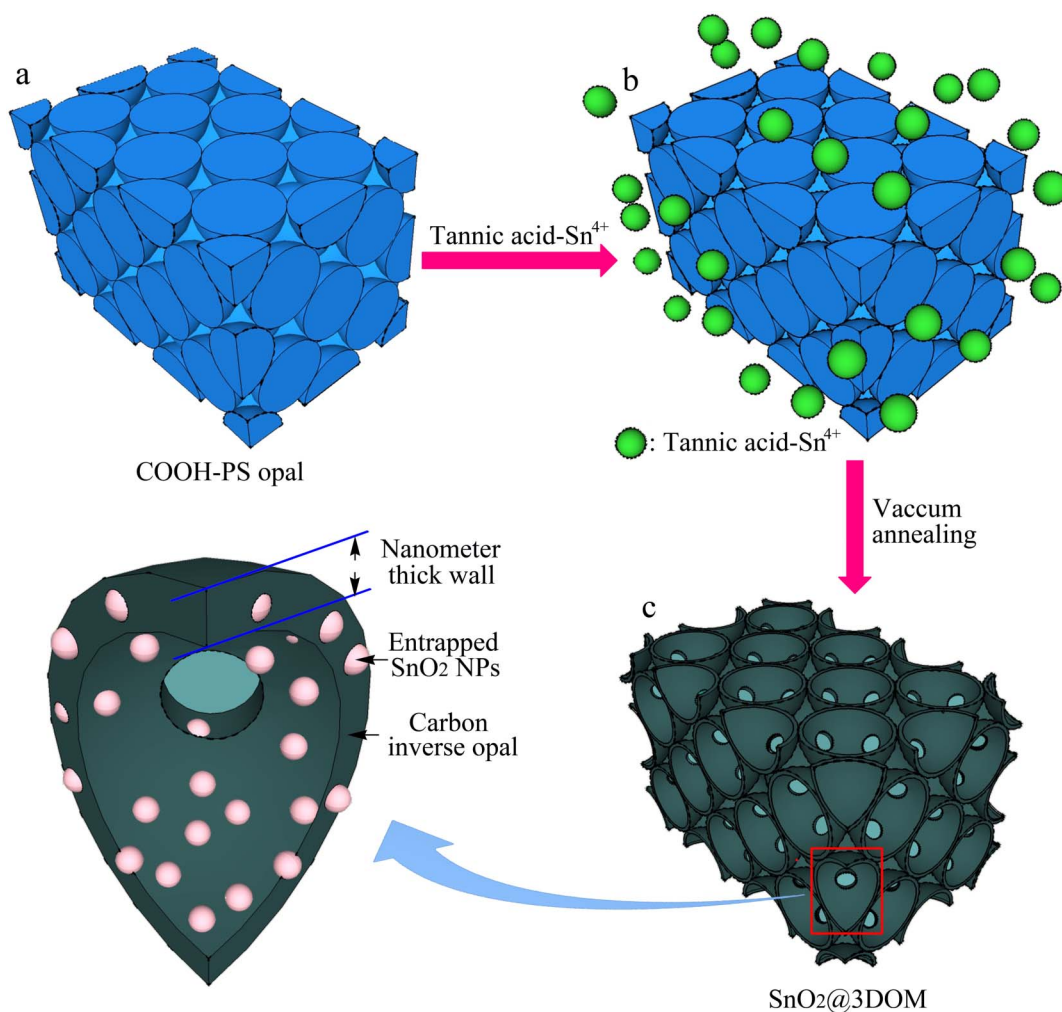


Figure 1 | Schematic illustration showing the preparation of SnO₂@3DOM electrode.

encapsulated in carbon shell³⁵, hybrid with carbon nanotube³⁶ or graphene³⁷. The cycling performance of 3DOM carbon inverse opal at a current density of 0.5 A g⁻¹ is also conducted while its reversible capacity during cycling is very limited (Supplementary Fig. S6), thus suggesting that the high reversible capacity of SnO₂@3DOM should be mainly derived from the SnO₂ nanoparticles. Compared with the electrodes that are prepared by direct coating SnO₂ on 3DOM carbon inverse opal (~200 mAh g⁻¹ in the 30th cycle), the SnO₂@3DOM still exhibits superior advantages both in capacity and cycling stability²⁴.

In general, poor charge transfer kinetics will lead to an increase in the impedance of batteries^{38,39}. To confirm that the entrapment of SnO₂ NPs in carbon inverse opal can be beneficial for charge transfer kinetics, we tested the electrochemical impedance spectroscopy (Figure 3c) of the SnO₂@3DOM after 3 and 500 cycles at a current density of 0.5 A g⁻¹, and an equivalent circuit was used for fitting the electrochemical impedance spectra. As shown in Figure 3c, the intercept at the Z' axis at high frequency corresponds to the ohmic resistance (R_Ω), which represents the total resistance of the electrolyte, separator and electrical contacts. The semicircle in the middle frequency range indicates the charge transfer resistance (R_{ct}), and the inclined line at lower frequency represents the Warburg impedance (W). Based on the model fitting, the charge transfer resistance (R_{ct}) is ~62 Ω after 3 cycles, which demonstrates the fast charge transfer kinetics in batteries. More interesting, the charge transfer resistance is further decreased to ~32 Ω after 500 cycles, corresponding to

improved charge transfer kinetics. Such phenomenon is also evident for the batteries based on CoO@3DOM electrode (see below in Figure 5c). These surprising results are due to the unique structure of the designed electrodes. Usually, the active materials will pulverize and peel off from the electrode at high current density, thus leading to significantly increased impedance. However, in SnO₂@3DOM, it is impossible for the SnO₂ NPs to substantially peel off from electrode because they are geometrically confined within the framework of the carbon inverse opal. Based on TEM analysis, the SnO₂ nanoparticles are still well entrapped in the carbon framework without serious aggregation even after 500 discharge/charge cycles (Supplementary Fig. S7), thus confirming that the 3DOM carbon framework indeed provides effective stabilization to the SnO₂ nanoparticles. Although the pulverization of SnO₂ NPs is inevitable during cycling, the electronic conductivity of the pulverized SnO₂ NPs with the carbon host can still be re-established during cycling, and therefore improved charge transfer kinetics with lower impedance can be exhibited. To further demonstrate this proposed mechanism, deep discharge/charge cycling of SnO₂@3DOM is carried out at even higher current density of 1.0 A g⁻¹ for 500 cycles, where the cracking and pulverization of SnO₂ will be more severe in the initial cycles. As shown in Figure 3b, the discharge capacity of SnO₂@3DOM at a current density of 1.0 A g⁻¹ initially exhibits a relatively more obvious decrease in the first dozens of cycles, but then steadily increases back in subsequent cycles, and gradually reaches equilibrium around the 470th cycle. Based on the proposed mechanism, these cycling behaviors are

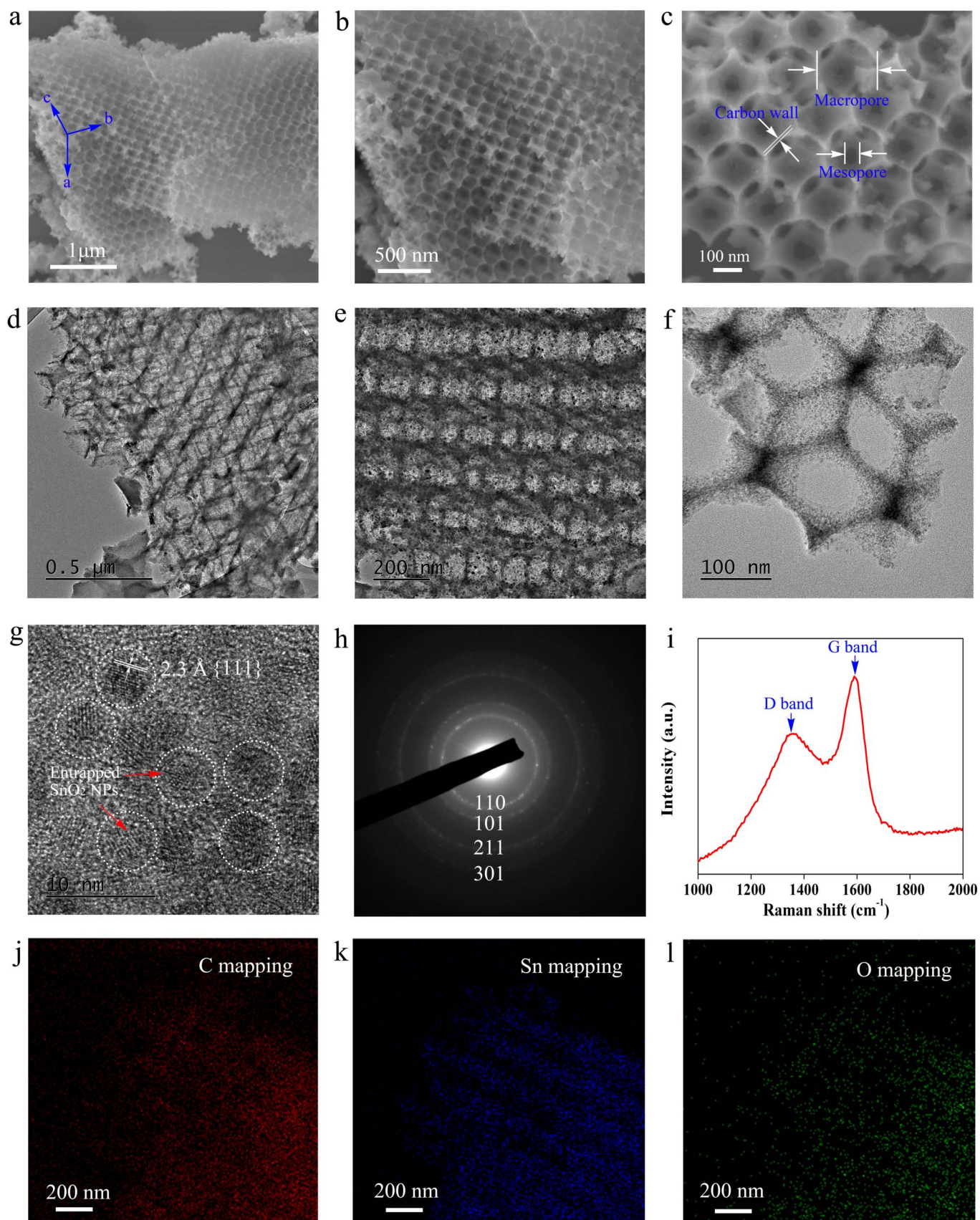


Figure 2 | Microstructure of $\text{SnO}_2@3\text{DOM}$ electrode.

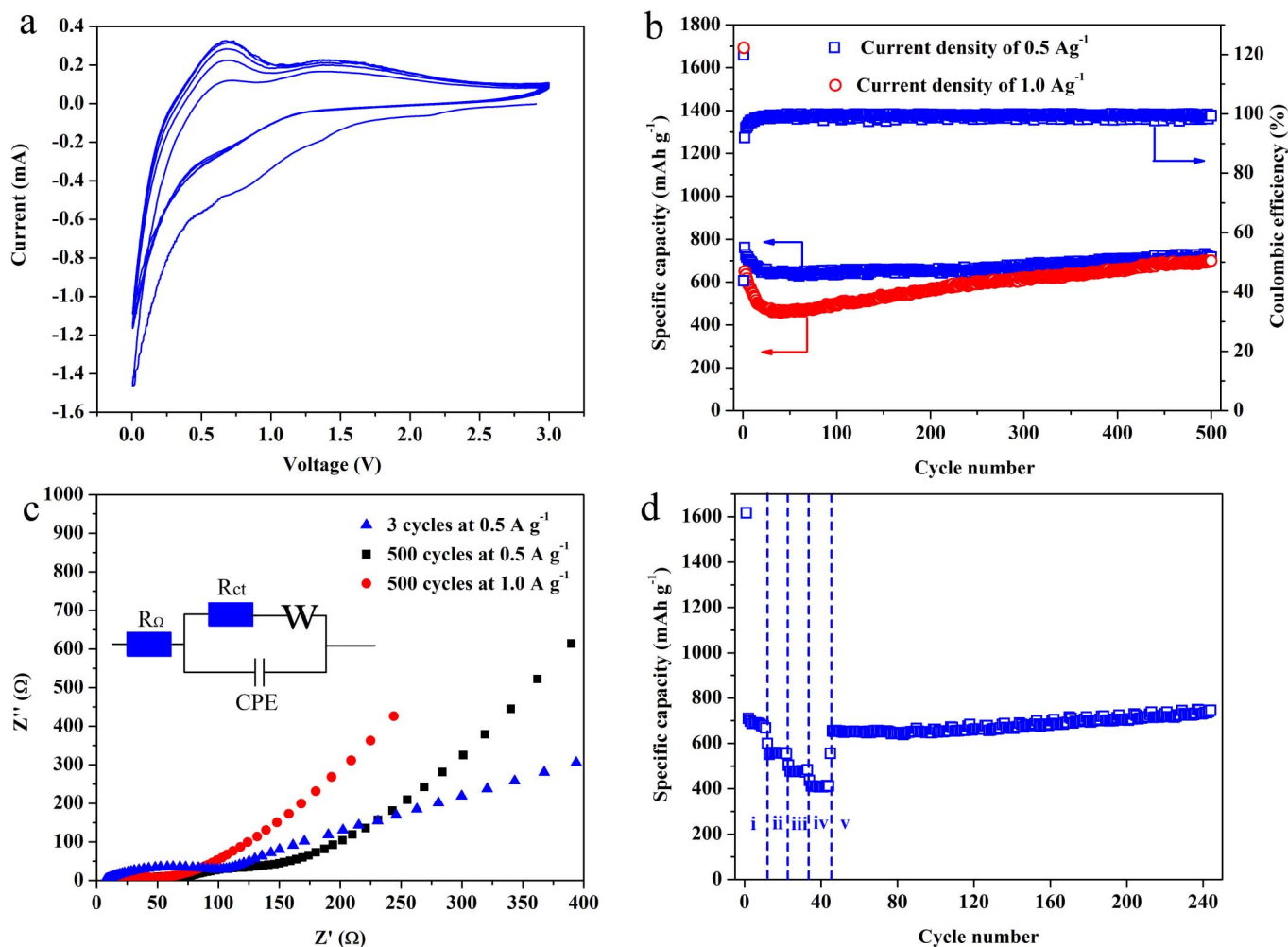


Figure 3 | Li-ion battery performances of $\text{SnO}_2@3\text{DOM}$.

reasonable and explainable. Compared with the cycling performances at 0.5 A g^{-1} , the more obvious capacity decrease at the initial stage is caused by the more severe pulverization of SnO_2 at the doubled current density (1.0 A g^{-1}). After that, the electronic conductivity of the pulverized particles with the carbon host is gradually re-establishing, and accordingly, the battery exhibits slow but steadily increased capacities with further cycling. Upon stable re-establishment of the electronic conductivity, the cycling performance of the $\text{SnO}_2@3\text{DOM}$ reaches equilibrium. Compared with the initial several cycles, the substantial decrease in impedance at 1.0 A g^{-1} after 500 cycles confirms the re-establishment of good charge-transfer (Figure 3c). Notably, the $\text{SnO}_2@3\text{DOM}$ delivers a high capacity of $\sim 700 \text{ mAh g}^{-1}$ in the 500th cycle at current density of 1.0 A g^{-1} . To the best of our knowledge, this is the longest reported lifespan under such high current density for SnO_2 -based anode materials used in LIBs.

Rate capability is another important criterion for high-performance LIBs. In Figure 3d, the rate capabilities of $\text{SnO}_2@3\text{DOM}$ were tested at current densities of 0.5, 1.0, 1.5 and 2.0 A g^{-1} , and the corresponding discharge capacities in the 10th cycle are 676.5, 556.7, 473.5 and 414.2 mAh g^{-1} , respectively. Notably, the discharge capacity of $\text{SnO}_2@3\text{DOM}$ could immediately increase back without any delay when the current density decreased from 2.0 to 0.5 A g^{-1} . The discharge capability maintains at 745.7 mAh g^{-1} in the 100th cycle, which shows that the well designed $\text{SnO}_2@3\text{DOM}$ can be operated under such current densities with pretty good rate capabilities. To further gain a measurement of the rate capability under conditions where fast ion and electron transport and structural stability of active materials should be essential, the discharge capability of

$\text{SnO}_2@3\text{DOM}$ is tested at different high current densities. As shown in Supplementary Fig. S8, the $\text{SnO}_2@3\text{DOM}$ delivers discharge capacities of 445.4, 368.2, 321.0, 285.8, 261.7, 216.0 and 147.5 mAh g^{-1} in the 50th cycle at the current densities of 1.0, 2.0, 3.0, 4.0, 5.0, 8.0 and 10.0 A g^{-1} , respectively. Upon returning the current density from 10.0 to 1.0 A g^{-1} , the discharge capacity can gradually increase back to $\sim 600 \text{ mAh g}^{-1}$ although there is some delay in capacity recovery. The significance of the above results strongly demonstrates that high-performance electrodes with outstanding stability and rate capability are possible by entrapping electrode active nanomaterials in macroporous carbon inverse opal.

Synthesis and characterization of the $\text{CoO}@3\text{DOM}$ electrode. Our strategy can be extended to synthesize other 3DOM electrodes because plant tannins have an outstanding chelating ability towards various transition metal ions^{40–43}. To verify this, we prepared $\text{CoO}@3\text{DOM}$ electrode by the same strategy as illustrated in Figure 1. XRD analysis demonstrates the presence of CoO in $\text{CoO}@3\text{DOM}$ (Supplementary Fig. S9), and the analysis of Raman spectroscopy confirms the formation of carbon framework (Supplementary Fig. S10). The morphology of periodic porosities, interconnected macropores on the order of 220 nm, and smaller mesopores on the order of 40–50 nm, are also evident in FE-SEM images shown in Figure 4a–c. The periodic porosity of the 3DOM electrode is clearly observed in Figure 4d, and the CoO NPs with diameter of $5 \sim 10 \text{ nm}$ are well entrapped in the 3DOM framework, as shown in Figure 4e. In Figure 4f, the CoO NPs with clear lattice fringes are confined in the carbon matrices without serious

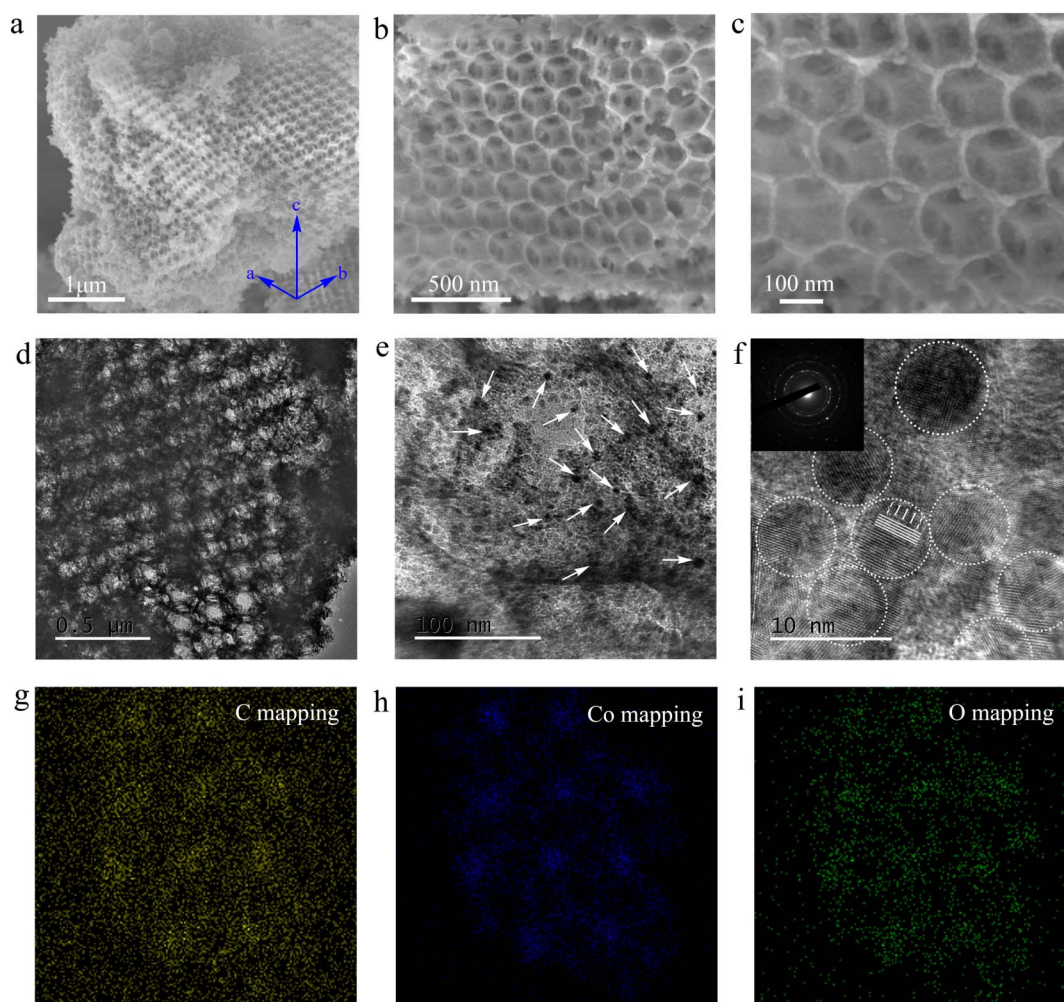


Figure 4 | Microstructure of CoO@3DOM.

aggregation, and the SAED analysis reveals their crystalline nature (inset in Figure 4f). Further EDX elemental mapping analyses confirm that the CoO NPs are successfully entrapped within the carbon inverse opal (Figure 4g–i). Moreover, the CoO@3DOM still exhibits low charge transfer resistance (R_{ct}) of 97 Ω (Figure 5c), thus revealing fast Li^+ diffusion and electron transfer kinetics.

Li-ion batteries performances of the CoO@3DOM electrode. The discharge/charge cycling performance of CoO@3DOM is first conducted at a current density of 0.5 A g^{-1} in the voltage range of 0.005–3.0 V. Figure 5a shows the galvanostatic discharge and charge voltage profiles generated by the CoO@3DOM in the 1st, 2nd and 500th cycles. In the 1st cycle, the discharge and charge of the CoO@3DOM occurs at 1375.5 and 736.7 mAh g^{-1} , respectively, and the coulombic efficiency is around 53.56%. In the 2nd cycle, the CoO@3DOM exhibits a reversible capacity of 718.6 mAh g^{-1} , and its coulombic efficiency is quickly increased to 94.58%. Notably, the discharge voltage profiles of the 500th and the 2nd cycles almost overlap with each other, suggesting a high cycling stability. Figure 5b shows the detailed cycling performances of CoO@3DOM. At a current density of 0.5 A g^{-1} , the discharge capacity just slightly decreases in the initial dozens of cycles and then steadily increases back, maintaining a high level of discharge capacity. In the 500th cycle, it delivers a capacity of 682.3 mAh g^{-1} , accounting for 95.43% of the theoretical capacity. At a current density of 2.0 A g^{-1} , the CoO@3DOM shows a more obvious capacity decrease in the initial cycles due to the more severe

pulverization of CoO at such high current density, and subsequently, the capacity gradually increase back and reaches an equilibration around the 400th cycle. In the 1000th cycle, CoO@3DOM can still deliver a high capacity of 673.7 mAh g^{-1} , accounting for 94.17% of the theoretical capacity. Hence, the CoO@3DOM also exhibits an excellent long-term cycling stability. Compared with the initial stage of cycling, the impedance of batteries substantially decreased from 97 to 28 Ω when cycled from the 3rd to 500th cycle at a current density of 0.5 A g^{-1} , as shown in Figure 5c. These changes of impedance are similar to those of batteries based on the SnO_2 @3DOM electrode, revealing the re-establishment of good charge transfer during discharge/charge cycling. According to the literature^{44,45}, other previous researches also reported the capacities of electrodes increase gradually after long term cycles, and they considered this might result from the improved Li-ion diffusion kinetics by an activation and stabilization process during cycling. Figure 5d shows the rate performance of the CoO@3DOM electrode at 1.0–10.0 A g^{-1} . The discharge capacities of the CoO@3DOM are 560.8, 479.9, 351.4, 297.8, 265.2, 238.9 and 200.6 mAh g^{-1} , respectively, when performed 50 cycles at 1.0, 2.0, 3.0, 4.0, 5.0, 8.0A and 10.0 A g^{-1} , respectively, and can gradually increase back to $\sim 590 \text{mAh g}^{-1}$ at 1.0 A g^{-1} . If the rate performance is conducted at relatively low current density (0.5–2.0 A g^{-1}), the capacity recovery will be faster when returning the discharge rate from a higher current density to a lower one (Supplementary Fig. S11). Again, the good electrochemical performances of the CoO@3DOM at high current densities demonstrate the feasibility of our strategy.

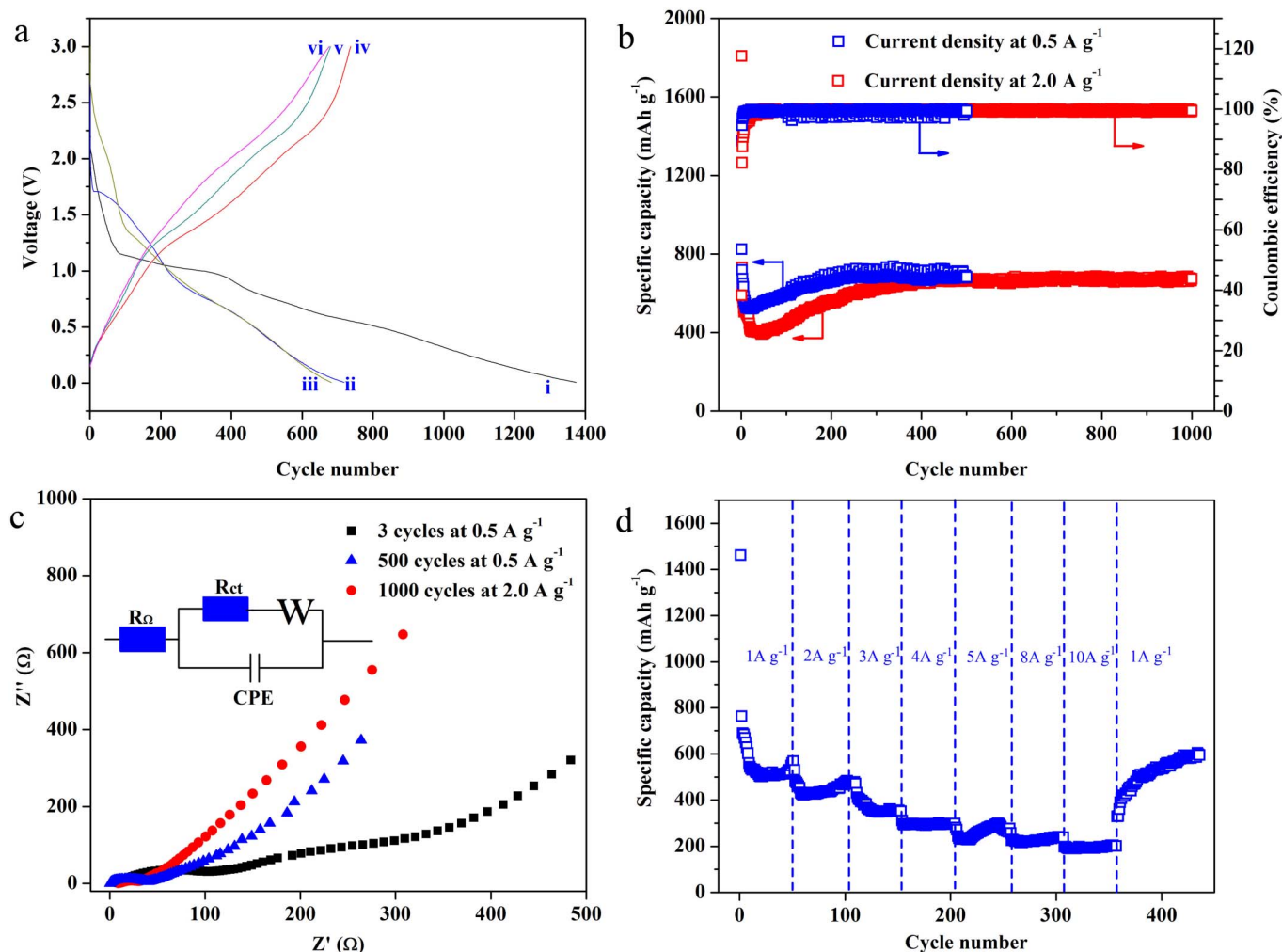


Figure 5 | Li-ion battery performances and electrochemical impedance spectroscopy of CoO@3DOM.

Discussion

In summary, we have demonstrated a versatile concept for the synthesis of three-dimensional ordered macroporous conductive electrode that displays a continuous and efficient pathway for fast ion and electron transport as well as stably geometrical constraints to active materials. This concept is established based on the integration of ordered macroporous carbon inverse opal with entrapped active nanoparticles. The carbon inverse opal not only serves as the interpenetrating continuous conductive network but also acts as a dimensional constraint to the active nanoparticles. The entrapment of the active nanoparticles provides intimate contact with the carbon inverse opal and also completely avoids the detachment problem of the active materials from the electrode, thus simultaneously affording fast ion and electron transport as well as superior cycling stability. These are vital to the success of all high-performance anodes to ensure large reversible capacity at high current densities. As demonstrated, the as-prepared electrode can deliver up to 94.17% of theoretical capacity over 1000 discharge/charge cycles, and exhibit excellent rate capability at the current density range of 1.0–10.0 A g⁻¹. It also should be noted that porous structured electrodes often suffer from relatively low volumetric energy density, and our 3D anode materials also have such problem because of their periodic macroporous structure. To elevate such problem, further improvements are still required. Owing to the flexibility of our concept, it is possible to fabricate a class of new high-performance electrodes previously considered not feasible due to their low electronic and

ionic conductivity, and we will report these researches in the forthcoming papers.

Methods

Opal template fabrication. The synthesis of carboxylic polystyrene (COOH-PS) spheres was fabricated as described previously^{46,47}. Typically, 100 ml of deionized water, 0.12 g of NaHCO₃, 5 ml of styrene and 0.5 ml of acrylic acid were added into a three-necked flask equipped with a reflux condenser and a mechanical stirrer where potassium persulfate served as the initiator. The reaction was carried out under a nitrogen atmosphere at 70 °C for 6 h, followed by reacting at 90 °C for 1 h. The resulting product was purified by centrifugation/dispersion cycles in water, and further aggregated to form self-assembled COOH-PS opal by high speed centrifugation.

SnO₂@3DOM fabrication. 0.02 g of tannic acid and 0.104 g of SnCl₄·xH₂O were mixed in 1.0 ml of deionized water. 0.05 g of COOH-PS opal was gently added to the above solution, followed by vacuum drying and thermal annealing in vacuum at 400 °C for 2.0 h.

CoO@3DOM fabrication. 0.02 g of tannic acid and 0.291 g of Co(NO₃)₂·6H₂O were mixed in 1.0 ml of deionized water. 0.05 g of COOH-PS opal was gently added to the above solution, followed by vacuum drying and thermal annealing in vacuum at 400 °C for 2.0 h.

3DOM carbon inverse opal. 0.02 g of tannic acid was mixed in 1.0 ml of deionized water. 0.05 g of COOH-PS opal was gently added to the above solution, followed by vacuum drying and thermal annealing in vacuum at 400 °C for 2.0 h.

Electrochemical measurement. Negative electrodes were comprised 70 wt% of SnO₂@3DOM (or CoO@3DOM), 20 wt% carbon nanotubes, and 10 wt% poly(vinylidene fluoride) binder. The anode materials were slurry-cast from N-



methyl-2-pyrrolidinone onto a Cu foil, and vacuum-dried at 50°C to completely remove the solvent. The electrochemical properties of the obtained working electrodes were measured using two-electrode CR2032 (3 V) coin-type cells with lithium foil serving as both counter and reference electrodes under ambient temperature. The electrolyte was 1 M LiPF₆ in a 50:50 (w/w) mixture of ethylene carbonate (EC) and dimethyl carbonate (DMC). Cell assembly was carried out in an argon-filled glove box with both moisture and oxygen contents below 1.0 ppm. Galvanostatic discharge/charge tests were performed using a NEWARE battery tester at a voltage window of 0.005–3.0 V. The specific capacity of the anode is calculated based on the mass of SnO₂@3DOM (or CoO@3DOM) contained in the anode composites. According to electrochemical tests, the discharge capacity contribution of carbon nanotubes to the SnO₂@3DOM (or CoO@3DOM) electrode is very limited (Supplementary Fig. S12).

Characterizations. Ultraviolet-visible (UV-vis) spectra analyses were conducted using UV-Vis spectrometer (Shimadzu UV-2501PC). Thermogravimetry analyses (TGA, Q500) were carried out in the temperature range 33–900°C at a heating rate of 15°C min⁻¹ in N₂ flow. Wide angle X-ray diffraction patterns of the samples were recorded using a Bruker D8 Advance diffractometer using Cu K α radiation. Raman spectra and images were obtained by a WITec CRM200 confocal microscopy Raman system with a piezocrystal controlled scanning stage. The morphology of the samples was characterized with a field emission scanning electron microscope (FESEM) system (JEOL, Model JSM-7600F) and a transmission electron microscope (TEM) system (JEOL, Model JEM-2010F) operating at 200 kV.

- Tarascon, J. M. & Armand, M. Issues and challenges facing rechargeable lithium batteries. *Nature* **414**, 359–367 (2001).
- Lee, S. W. *et al.* High-power lithium batteries from functionalized carbon-nanotube electrodes. *Nat. Nanotech.* **5**, 531–537 (2010).
- Chan, C. K. *et al.* High-performance lithium battery anodes using silicon nanowires. *Nat. Nanotech.* **3**, 31–35 (2008).
- Kim, M. G. & Cho, J. Reversible and high-capacity nanostructured electrode materials for Li-ion batteries. *Adv. Funct. Mater.* **19**, 1497–1514 (2009).
- Zhang, H. G., Yu, X. D. & Braun, P. V. Three-dimensional bicontinuous ultrafast-charge and -discharge bulk battery electrodes. *Nat. Nanotech.* **6**, 277–281 (2011).
- Liang, S. Z., Zhu, X. F., Lian, P. C., Yang, W. S. & Wang, H. H. Superior cycle performance of Sn@C/graphene nanocomposite as an anode material for lithium-ion batteries. *J. Solid State Chem.* **184**, 1400–1404 (2011).
- Arico, A. S., Bruce, P., Scrosati, B., Tarascon, J. M. & Van Schalkwijk, W. Nanostructured materials for advanced energy conversion and storage devices. *Nat. Mater.* **4**, 366–377 (2005).
- Wu, Z. S. *et al.* Graphene anchored with Co₃O₄ nanoparticles as anode of lithium ion batteries with enhanced reversible capacity and cyclic performance. *ACS nano* **4**, 3187–3194 (2010).
- Yang, S. B. *et al.* Porous iron oxide ribbons grown on graphene for high-performance lithium storage. *Sci. Rep.* **2**, (2012).
- Poizot, P., Laruelle, S., Grugeon, S., Dupont, L. & Tarascon, J. M. Nano-sized transition-metal oxides as negative-electrode materials for lithium-ion batteries. *Nature* **407**, 496–499 (2000).
- Zhang, W. J. A review of the electrochemical performance of alloy anodes for lithium-ion batteries. *J. Power Sources* **196**, 13–24 (2011).
- Li, H. Q. & Zhou, H. S. Enhancing the performances of Li-ion batteries by carbon-coating: present and future. *Chem. Commun.* **48**, 1201–1217 (2012).
- Qiu, Y. C., Yan, K. Y. & Yang, S. H. Ultrafine tin nanocrystallites encapsulated in mesoporous carbon nanowires: scalable synthesis and excellent electrochemical properties for rechargeable lithium ion batteries. *Chem. Commun.* **46**, 8359–8361 (2010).
- Chockla, A. M. *et al.* Silicon nanowire fabric as a lithium ion battery electrode material. *J. Am. Chem. Soc.* **133**, 20914–20921 (2011).
- Wang, N., Xu, J. X. & Guan, L. X. Synthesis and enhanced photocatalytic activity of tin oxide nanoparticles coated on multi-walled carbon nanotube. *Mater. Res. Bull.* **46**, 1372–1376 (2011).
- Bonino, C. A. *et al.* Electrospun carbon-tin oxide composite nanofibers for use as lithium ion battery anodes. *ACS Appl. Mater. Interfaces* **3**, 2534–2542 (2011).
- Zhu, X. J., Zhu, Y. W., Murali, S., Stollers, M. D. & Ruoff, R. S. Nanostructured reduced graphene Oxide/Fe₂O₃ composite as a high-performance anode material for lithium ion batteries. *ACS Nano* **5**, 3333–3338 (2011).
- Luo, B. *et al.* Graphene-confined Sn nanosheets with enhanced lithium storage capability. *Adv. Mater.* **24**, 3538–3543 (2012).
- Amin, R., Balaya, P. & Maier, J. Anisotropy of electronic and ionic transport in LiFePO₄ single crystals. *Electrochem. Solid-State Lett.* **10**, A13–A16 (2007).
- Lytle, J. C., Yan, H. W., Ergang, N. S., Smyrl, W. H. & Stein, A. Structural and electrochemical properties of three-dimensionally ordered macroporous tin(IV) oxide films. *J. Mater. Chem.* **14**, 1616–1622 (2004).
- Timothy, S. *et al.* Three-dimensional electrodes and battery architectures. *MRS Bull.* **36**, 523–531 (2011).
- Sorensen, E. M. *et al.* Three-dimensionally ordered macroporous Li₄Ti₅O₁₂: effect of wall structure on electrochemical properties. *Chem. Mater.* **18**, 482–489 (2006).
- Kavan, L., Zukalova, M. T., Kalbac, M. & Graetzel, M. Lithium insertion into anatase inverse opal. *J. Electrochem. Soc.* **151**, A1301–A1307 (2004).
- Lee, K. T., Lytle, J. C., Ergang, N. S., Oh, S. M. & Stein, A. Synthesis and rate performance of monolithic macroporous carbon electrodes for lithium-ion secondary batteries. *Adv. Funct. Mater.* **15**, 547–556 (2005).
- Esmanski, A. & Ozin, G. A. Silicon inverse-opal-based macroporous materials as negative electrodes for lithium ion batteries. *Adv. Funct. Mater.* **19**, 1999–2010 (2009).
- Landon, P. B., Gilleland, C. L. & Glosser, R. Properties of metallo-dielectric opals and metallic inverse opal photonic crystals. *J. Mater. Sci. : Mater. Electron.* **18**, S469–S472 (2007).
- Orilall, M. C., Abrams, N. M., Lee, J., DiSalvo, F. J. & Wiesner, U. Highly crystalline inverse opal transition metal oxides via a combined assembly of soft and hard chemistries. *J. Am. Chem. Soc.* **130**, 8882–8883 (2008).
- Guan, G. Q. *et al.* Preferential CO oxidation over catalysts with well-defined inverse opal structure in microchannels. *Int. J. Hydrogen Energy* **33**, 797–801 (2008).
- Vu, A., Qian, Y. Q. & Stein, A. Porous electrode materials for lithium-ion batteries – how to prepare them and what makes them special. *Adv. Energy Mater.* **2**, 1056–1085 (2012).
- Huang, J. H., Liu, Y. F. & Wang, X. G. Selective adsorption of tannin from flavonoids by organically modified attapulgite clay. *J. Hazard. Mater.* **160**, 382–387 (2008).
- Lin, D. H. & Xing, B. S. Tannic acid adsorption and its role for stabilizing carbon nanotube suspensions. *Environ. Sci. Technol.* **42**, 5917–5923 (2008).
- Lou, X. W., Li, C. M. & Archer, L. A. Designed synthesis of coaxial SnO₂@carbon hollow nanospheres for highly reversible lithium storage. *Adv. Mater.* **21**, 2536–2539 (2009).
- Zhu, X. J., Zhu, Y. W., Murali, S., Stoller, M. D. & Ruoff, R. S. Reduced graphene oxide/tin oxide composite as an enhanced anode material for lithium ion batteries prepared by homogenous coprecipitation. *J. Power Sources* **196**, 6473–6477 (2011).
- Yin, X. M. *et al.* One-step synthesis of hierarchical SnO₂ hollow nanostructures via self-assembly for high power lithium ion batteries. *J. Phys. Chem. C* **114**, 8084–8088 (2010).
- Lee, K. T., Jung, Y. S. & Oh, S. M. Synthesis of tin-encapsulated spherical hollow carbon for anode material in lithium secondary batteries. *J. Am. Chem. Soc.* **125**, 5652–5653 (2003).
- Fu, Y. B., Ma, R. B., Shu, Y., Cao, Z. & Ma, X. H. Preparation and characterization of SnO₂/carbon nanotube composite for lithium ion battery applications. *Mater. Lett.* **63**, 1946–1948 (2009).
- Li, Y. M., Lv, X. J., Lu, J. & Li, J. H. Preparation of SnO₂-nanocrystal/graphene-nanosheets composites and their lithium storage ability. *J. Phys. Chem. C* **114**, 21770–21774 (2010).
- Szczeczek, J. R. & Jin, S. Nanostructured silicon for high capacity lithium battery anodes. *Energy Environ. Sci.* **4**, 56–72 (2011).
- Wu, H. *et al.* Aligned NiO nanoflake arrays grown on copper as high capacity lithium-ion battery anodes. *J. Mater. Chem.* **22**, 19821–19825 (2012).
- Quideau, S., Deffieux, D., Douat-Casassus, C. & Pouysegou, L. Plant polyphenols: chemical properties, biological activities, and synthesis. *Angew. Chem. Int. Ed.* **50**, 586–621 (2011).
- Ma, H. W., Liao, X. P., Liu, X. & Shi, B. Recovery of platinum(IV) and palladium(II) by bayberry tannin immobilized collagen fiber membrane from water solution. *J. Membr. Sci.* **278**, 373–380 (2006).
- Mao, H., Ma, J., Liao, Y., Zhao, S. L. & Liao, X. P. Using plant tannin as natural amphiphilic stabilizer to construct an aqueous-organic biphasic system for highly active and selective hydrogenation of quinoline. *Catal. Sci. Technol.* **3**, 1612–1617 (2013).
- Nakano, Y., Takeshita, K. & Tsutsumi, T. Adsorption mechanism of hexavalent chromium by redox within condensed-tannin gel. *Water Res.* **35**, 496–500 (2001).
- Zeng, L. X., Zheng, C., Xia, L. C., Wang, Y. X. & Wei, M. D. Ordered mesoporous TiO₂-C nanocomposite as an anode material for long-term performance lithium-ion batteries. *J. Mater. Chem. A* **1**, 4293–4299 (2013).
- Zeng, L. X. *et al.* ZnV₂O₄-CMK nanocomposite as an anode material for rechargeable lithium ion batteries. *J. Mater. Chem.* **22**, 14284–14288 (2012).
- Lu, Z. Y. *et al.* Monodisperse magnetizable silica composite particles from heteroaggregate of carboxylic polystyrene latex and Fe₃O₄ nanoparticles. *Nanotechnology* **19**, 055602 (2008).
- Wang, P. H. & Pan, C. Y. Preparation of styrene/acrylic acid copolymer microspheres: polymerization mechanism and carboxyl group distribution. *Colloid Polym. Sci.* **280**, 152–159 (2002).

Acknowledgements

This work was supported by Singapore Ministry of Education (MOE2010-T2-1-017), A*STAR SERC grant 1021700144, NRF2009EWT-CERP001-026 (Singapore), Singapore National Research Foundation under CREATE program: EMobility in Megacities, and Singapore MPA 23/04.15.03 RDP 020/10/113 grant.

Author contributions

X. H. and H. H. H. conceived the idea. X. H. and Z. L. carried out materials fabrication. X. H., J. C. and H. Y. performed materials characterizations and electrochemical tests. X. H.,



H. H. H. and Q. Y. drafted the manuscript. All authors analyzed and discussed the experimental results.

Additional information

Supplementary information accompanies this paper at <http://www.nature.com/scientificreports>

Competing financial interests: The authors declare no competing financial interests.

How to cite this article: Huang, X. *et al.* Carbon inverse opal entrapped with electrode active nanoparticles as high-performance anode for lithium-ion batteries. *Sci. Rep.* 3, 2317; DOI:10.1038/srep02317 (2013).



This work is licensed under a Creative Commons Attribution-NonCommercial-NoDerivs 3.0 Unported license. To view a copy of this license, visit <http://creativecommons.org/licenses/by-nc-nd/3.0>